# Remote Generation of Modulators for Super-Resolution Imaging

Jian-yu  $\mathrm{Lu}^1$ 

<sup>1</sup>Department of Bioengineering, The University of Toledo

September 15, 2025

# Remote Generation of Modulators for Super-Resolution Imaging

Jian-yu Lu

Department of Bioengineering, The University of Toledo, Toledo, Ohio, USA Email: <u>jian-yu.lu@ieee.org</u>

# **ABSTRACT**

In 1873, Ernst Abbe found a diffraction limited resolution of about 200 nm for conventional optical microscopes. Many methods to overcome the limit (super-resolution) have been developed. Recently, a general super-resolution imaging method was developed based on the theory of linear shift-invariant (LSI) system and modulation of the system point-spread-function (PSF) (Lu, IEEE TUFFC, Jan. 2024), which has broad applications in various disciplines of science, engineering, and medicine. In this paper, focused shear waves generated remotely by radiation force were studied comprehensively via theoretical analyses and computer simulations to modulate the imaging waves or the PSF of imaging systems such as those of B-mode and photoacoustics for super-resolution imaging. A method to reduce sidelobes and thus increase the contrast of super-resolution images was developed. Atomic imaging with small physical particles such as optically opaque ions was suggested. It is found that focused shear waves can be produced with an annular, 2D, or 1D array transducer; with a conventional focused beam; or even with local vibration sources. Also, they can resonate to increase signal-to-noise ratio (SNR). This study paves a way for super-resolution imaging of mechanical properties (shear-wave amplitude, speed, spectrum, and nonlinearity) of biological soft tissues deep in the body.

# 1.INTRODUCTION

In 1873, Ernst Abbe found that the conventional optical microscopes have a diffraction limited resolution of about 200 nm [1]. Methods to overcome the limit (super-resolution) have been developed [2]-[12], including the 1994 stimulated emission depletion (STED) [13] and 2006 photoactivated localization microscopy (PALM) [14] that won the 2014 Nobel Prize in Chemistry. Recently, a general super-resolution imaging method was developed by the author based on the theory of linear shift-invariant (LSI) system and modulation of the system point spread function (PSF) [15]. Since many practical imaging systems are LSI or can be approximated as an LSI system, the method can have broad applications in various disciplines of science, engineering, and medicine [15]-[18]. In this paper, focused shear waves were studied in details as modulators both theoretically and with computer simulations for low-sidelobe and high-contrast super-resolution imaging of mechanical properties (shear-wave amplitude, speed, spectrum, and nonlinearity) of biological soft tissues deep in the body if the half wavelength of the shear waves is smaller than the size of the PSF. The focused shear waves can be produced remotely by focused Bessel (forming a cylindrical ring of radiation force [19]-[21]) or cosine [22] (forming plates of radiation force) beams with an annular (can be steered mechanically [20]), 2D, or 1D array transducer or produced locally by other vibration sources to modulate the imaging waves or the PSF of imaging systems such as pulse-echo B-mode, photoacoustic [23], and non-destructive evaluation (NDE) [24] imaging. Note that since the conventional focused plane wave is a special case of the focused Bessel or cosine beam with their scaling parameters set to zero [20], it also can be used to produce focused shear waves for super-resolution imaging, which minimizes the effects of shear wave attenuation [25]. Also, the focused shear waves can produce high resonance peaks under certain boundary conditions, which increases shear-wave amplitude for imaging of nonlinear properties of objects and improving the signal-to-noise ratio (SNR) of the imaging systems. Such boundary conditions can be realized with phased-locked radiation force [26], fixed amplitude or stress at the boundaries, or other mechanisms [27]. Finally, the sensitivity and dynamic range of the imaging systems, and thus the resolution of super-resolution images, can be greatly increased if the imaging waves modulated at different times can interfere coherently before being detected using the block diagram in the lower-left corner of Fig. 1 (also see P. 167 of Ref. [15]). In addition to the focused shear waves, the modulators can be small physical particles such as nanoparticles (or may be optically opaque ions for atomic imaging) [15].

#### 2. THEORETICAL PRELIMINARIES

#### A. NAVIER-CAUCHY EQUATION FOR ISOTROPIC AND LINEAR ELASTICITY

The Newton's second law for a small volume of material (equation of motion) is given by [27]:

$$\rho(\vec{r};t)\frac{\partial^2 \vec{s}'(\vec{r};t)}{\partial t^2} = \nabla \cdot \mathbf{\sigma}(\vec{r};t) + \vec{q}'(\vec{r};t), \qquad (1)$$

where  $\rho(\vec{r};t)$  is density (kg/m³),  $\vec{s}'(\vec{r};t)$  is displacement in meter (m), " $\nabla$ ·" is the divergence in terms of  $\vec{r}$ ,  $\sigma(\vec{r};t)$  is a stress tensor (Pascal or Pa or N/m²),  $\vec{q}'(\vec{r};t)$  is a force per unit volume or volumetric force (N/m³),  $\vec{r} = (x_0, y_0, z)$  is a spatial position in rectangular coordinates (see Fig. 1), and t is the time. According to Hooke's Law (stress-strain relationship) in isotropic linear elastic media, we have [27]:

$$\sigma(\vec{r};t) = \gamma [\nabla \cdot \vec{s}'(\vec{r};t)] \mathbf{I} + 2\mu \epsilon(\vec{r};t), \qquad (2)$$

where  $\gamma$  (N/m<sup>2</sup>) is the first Lame constant,  $\mu$  (N/m<sup>2</sup>) is the second Lame constant or shear module, **I** is a unit (identity) tensor, and  $\varepsilon(\vec{r};t)$  is a strain tensor (a relative dimension change):

$$\mathbf{\varepsilon}(\vec{r};t) = \{\nabla \vec{s}'(\vec{r};t) + [\nabla \vec{s}'(\vec{r};t)]^T\}/2, \tag{3}$$

where  $\nabla$  is a gradient in terms of  $\vec{r}$ , and T means transpose. Inserting Eqs. (2) and Eq. (3) into Eq. (1), we obtain the Navier-Cauchy equation for isotropic and linear elasticity if the media is approximately incompressible (i.e.,  $\nabla \cdot \vec{s}$  ' $(\vec{r};t) \approx 0$ , in media such as biological soft tissues):

$$\rho(\vec{r};t)\frac{\partial^{2}\vec{s}'(\vec{r};t)}{\partial t^{2}} = \nabla \cdot \{\gamma[\nabla \cdot \vec{s}'(\vec{r};t)]\mathbf{I} + 2\mu\mathbf{\epsilon}(\vec{r};t)\} + \vec{q}'(\vec{r};t) = \gamma\nabla[\nabla \cdot \vec{s}'(\vec{r};t)] + \mu\nabla^{2}\vec{s}'(\vec{r};t) + \mu\nabla[\nabla \cdot \vec{s}'(\vec{r};t)] + \vec{q}'(\vec{r};t)$$

$$= \mu\nabla^{2}\vec{s}'(\vec{r};t) + (\gamma + \mu)\nabla[\nabla \cdot \vec{s}'(\vec{r};t)] + \vec{q}'(\vec{r};t) \approx \mu\nabla^{2}\vec{s}'(\vec{r};t) + \vec{q}'(\vec{r};t)$$

$$(4)$$

or

$$\nabla^2 \vec{s} \,'(\vec{r};t) - \frac{1}{\mu/\rho(\vec{r};t)} \frac{\partial^2 \vec{s} \,'(\vec{r};t)}{\partial t^2} = -\frac{\vec{q} \,'(\vec{r};t)}{\mu} \Rightarrow \nabla^2 \vec{s} \,'(\vec{r};t) - \frac{1}{c_s^2(\vec{r};t)} \frac{\partial^2 \vec{s} \,'(\vec{r};t)}{\partial t^2} = -\frac{\vec{q} \,'(\vec{r};t)}{\mu} \,, \tag{5}$$

where  $c_s(\vec{r};t) = \sqrt{\mu/\rho(\vec{r};t)}$  is the shear wave speed (m/s), where the subscript "s" means shear wave.

In cylindrical coordinates, Eq. (5) is given by:

$$\left[ \frac{1}{r_0} \frac{\partial}{\partial r_0} (r_0 \frac{\partial}{\partial r_0}) + \frac{1}{r_0^2} \frac{\partial^2}{\partial \phi_0^2} + \frac{\partial^2}{\partial z^2} - \frac{1}{c_s^2 (\vec{r};t)} \frac{\partial^2}{\partial t^2} \right] \vec{s}(r_0, \phi_0, z;t) = -\frac{\vec{q}(r_0, \phi_0, z;t)}{\mu}, \tag{6}$$

where  $\vec{s}(r_0, \phi_0, z; t) = \vec{s}'(\vec{r}; t)$ ,  $\vec{q}(r_0, \phi_0, z; t) = \vec{q}'(\vec{r}; t)$ ,  $r_0 = \sqrt{x_0^2 + y_0^2}$  is the radial distance,  $\phi_0$  is the azimuthal angle,  $x_0 = r_0 \cos(\phi_0)$ ,  $y_0 = r_0 \sin(\phi_0)$ ,  $\vec{r} = (r_0 \cos(\phi_0), r_0 \sin(\phi_0), z)$ .

#### **B.SOLUTIONS TO THE WAVE EQUATION**

#### I. SHEAR WAVE PRODUCTION WITH CYLINDRICAL RING OF RADIATION FORCE

#### a. Solutions by Directly Solving the Wave Equation:

Assuming that  $c_s(\vec{r};t) = c_s$  is a constant (which means that  $\rho(\vec{r};t)$  is a constant if  $\mu$  is a constant), the shear wave displacement  $\vec{s}(r_0,\phi_0,z;t)$  and the external volumetric force  $\vec{q}(r_0,\phi_0,z;t)$  are not a function of both  $\phi_0$  and z, and these vectors have only the z component, i.e.,  $\vec{s}(r_0,\phi_0,z;t) = s(r_0,\phi_0,z;t)\vec{z}^0 = s(r_0;t)\vec{z}^0$  and  $\vec{q}(r_0,\phi_0,z;t) = q(r_0,\phi_0,z;t)\vec{z}^0 = q(r_0;t)\vec{z}^0$ , where  $\vec{z}^0$  is a unit vector in z, Eq. (6) can be simplified:

$$\left[\frac{1}{r_0}\frac{\partial}{\partial r_0}(r_0\frac{\partial}{\partial r_0}) - \frac{1}{c_s^2}\frac{\partial^2}{\partial t^2}\right]s(r_0;t) = -\frac{q(r_0;t)}{\mu}.$$
 (7)

If the external volumetric force is sinusoidal with frequency,  $f_s$  (angular frequency  $\omega_s = 2\pi f_s$ ), i.e.,  $q(r_0;t) = Q(r_0)e^{-i\omega_s t}$  and  $s(r_0;t) = S(r_0;\omega_s)e^{-i\omega_s t}$ , where  $i=\sqrt{-1}$ , the subscript "s" of  $f_s$  and  $\omega_s$  represents shear wave, and the amplitude of the volumetric force is uniform within the cylindrical ring, i.e.,  $Q(r_0) = Q_0$  is a constant for  $0 < d_1 \le r_0 \le d_2$ , and  $Q(r_0) = 0$  elsewhere, Eq. (7) becomes the following inhomogeneous Helmholtz equation:

$$\left[\frac{1}{r_0}\frac{\partial}{\partial r_0}(r_0\frac{\partial}{\partial r_0}) - \frac{1}{c_s^2}\frac{\partial^2}{\partial t^2}\right]S(r_0;\omega_s)e^{-i\omega_s t} = -\frac{Q(r_0)e^{-i\omega_s t}}{\mu} \Rightarrow \frac{d^2S(r_0;\omega_s)}{dr_0^2} + \frac{1}{r_0}\frac{dS(r_0;\omega_s)}{dr_0} + k_s^2S(r_0;\omega_s) = \begin{cases} -\frac{Q_0}{\mu}, & 0 < d_1 \le r_0 \le d_2 \\ 0, & \text{Otherwise} \end{cases}, (8)$$

where  $d_1$  and  $d_2$  are the inner and outer radii of the cylindrical ring respectively, and  $k_s = \omega_s / c_s$  is the wave number of the shear wave ( $k_s$  is a complex number if there is attenuation). General solutions to Eq. (8) can be obtained by getting a general solution to the homogeneous Helmholtz equation (setting the right hand side of Eq. (8) to zero) plus a specific solution to the inhomogeneous Helmholtz equation. Letting  $\xi_0 = k_s r_0$  and  $S(r_0; \omega_s) = S'(\xi_0; \omega_s)$ , the homogeneous Helmholtz equation in Eq. (8) becomes a zeroth-order Bessel equation:

$$r_0^2 \frac{d^2 S(r_0; \omega_s)}{dr_0^2} + r_0 \frac{d S(r_0; \omega_s)}{dr_0} + k_s^2 r_0^2 S(r_0; \omega_s) = 0 \Rightarrow \xi_0^2 \frac{d^2 S'(\xi_0; \omega_s)}{d\xi_0^2} + \xi_0 \frac{d S'(\xi_0; \omega_s)}{d\xi_0} + \xi_0^2 S'(\xi_0; \omega_s) = 0.$$
 (9)

Thus, the general solutions to Eq. (8) are given by linear combinations of zeroth-order Bessel functions:

$$S(r_0; \omega_s) = S'(\xi_0; \omega_s) = \begin{cases} A_0 J_0(k_s r_0), & 0 \le r_0 < d_1 \\ B_0 J_0(k_s r_0) + C_0 Y_0(k_s r_0) - Q_0 / (k_s^2 \mu), & d_1 \le r_0 \le d_2 , \\ D_0 H_0^{(1)}(k_s r_0), & r_0 > d_2 \end{cases}$$

$$(10)$$

where  $-Q_0/(k_s^2\mu)$  is a specific solution to Eq. (8) in the region  $d_1 \le r_0 \le d_2$ ,  $J_0(k_s r_0)$  and  $Y_0(k_s r_0)$  are the zeroth-order Bessel functions of the first and second kind respectively  $(Y_0(k_s r_0))$  is also called zeroth-order Neumann

function), and  $H_0^{(1)}(k_s r_0) = J_0(k_s r_0) + i Y_0(k_s r_0)$  is the zeroth-order Hankel function of the first kind for an outgoing wave since its asymptotic behavior is  $H_0^{(1)}(k_s r_0) \to \sqrt{2/(\pi k_s r_0)} e^{i(k_s r_0 - \pi/4)}$  as  $k_s r_0 \to \infty$ . Note that the coefficient of  $Y_0(k_s r_0)$  for  $r_0 < d_1$  is set to zero in Eq. (10) (i.e.,  $S(r_0; \omega_s) = A_0 J_0(k_s r_0)$ ) since  $|Y_0(k_s r_0)| \to \infty$  as  $r_0 \to 0$ . As for  $r_0 > d_2$ ,  $H_0^{(1)}(k_s r_0)$  instead of  $J_0(k_s r_0)$  and  $Y_0(k_s r_0)$  is used because the latter two represent standing waves.

Applying the continuity boundary conditions on both the displacement and stress (proportional to the radial derivative of the displacement according to the Hooke's law in isotropic linear elastic media) in Eq. (10), we have:

$$\begin{cases} (1) \text{ At } r_0 = d_1 \text{ (Displacement Continuity): } & A_0 J_0(k_s d_1) = B_0 J_0(k_s d_1) + C_0 Y_0(k_s d_1) - Q_0/(k_s^2 \mu) \\ (2) \text{ At } r_0 = d_1 \text{ (Radial Stress Continuity): } & d[A_0 J_0(k_s r_0)]/dr_0|_{r_0 = d_1} = d[B_0 J_0(k_s r_0) + C_0 Y_0(k_s r_0)]/dr_0|_{r_0 = d_1} \\ (3) \text{ At } r_0 = d_2 \text{ (Displacement Continuity): } & B_0 J_0(k_s d_2) + C_0 Y_0(k_s d_2) - Q_0/(k_s^2 \mu) = D_0 H_0^{(1)}(k_s d_2) \\ (4) \text{ At } r_0 = d_2 \text{ (Radial Stress Continuity): } & d[B_0 J_0(k_s r_0) + C_0 Y_0(k_s r_0)]/dr_0|_{r_0 = d_2} = d[D_0 H_0^{(1)}(k_s r_0)]/dr_0|_{r_0 = d_2} \\ \Rightarrow (1) A_0 J_0(k_s d_1) - B_0 J_0(k_s d_1) - C_0 Y_0(k_s d_1) = -Q_0/(k_s^2 \mu); & (2) A_0 J_1(k_s d_1) - B_0 J_1(k_s d_1) - C_0 Y_1(k_s d_1) = 0; & . \end{cases} \tag{11}$$

$$(3) B_0 J_0(k_s d_2) + C_0 Y_0(k_s d_2) - D_0 H_0^{(1)}(k_s d_2) = Q_0/(k_s^2 \mu); & (4) B_0 J_1(k_s d_2) + C_0 Y_0(k_s d_2) - D_0 H_1^{(1)}(k_s d_2) = 0$$

Eq. (11) can be written in a matrix form, i.e.:

$$\mathbf{A}\mathbf{x} = \mathbf{b} \Rightarrow \mathbf{A} = \begin{bmatrix} J_0(k_s d_1) & -J_0(k_s d_1) & -Y_0(k_s d_1) & 0 \\ J_1(k_s d_1) & -J_1(k_s d_1) & -Y_1(k_s d_1) & 0 \\ 0 & J_0(k_s d_2) & Y_0(k_s d_2) & -H_0^{(1)}(k_s d_2) \\ 0 & J_1(k_s d_2) & Y_1(k_s d_2) & -H_1^{(1)}(k_s d_2) \end{bmatrix}, \mathbf{x} = \begin{bmatrix} A_0 \\ B_0 \\ C_0 \\ D_0 \end{bmatrix}, \mathbf{b} = \begin{bmatrix} -Q_0/(k_s^2 \mu) \\ 0 \\ Q_0/(k_s^2 \mu) \\ 0 \end{bmatrix}.$$
(12)

Solving Eq. (12), we obtain the coefficients  $A_0, B_0, C_0$ , and  $D_0$  of the shear wave in Eq. (10):

$$\begin{cases}
A_{0} = [i\pi Q_{0}/(2k_{s}\mu)][d_{2}H_{1}^{(1)}(k_{s}d_{2}) - d_{1}H_{1}^{(1)}(k_{s}d_{1})] \\
B_{0} = [i\pi Q_{0}/(2k_{s}\mu)][-d_{1}J_{1}(k_{s}d_{1}) + d_{2}H_{1}^{(1)}(k_{s}d_{2})] \\
C_{0} = [\pi Q_{0}/(2k_{s}\mu)]d_{1}J_{1}(k_{s}d_{1}) \\
D_{0} = [i\pi Q_{0}/(2k_{s}\mu)][-d_{1}J_{1}(k_{s}d_{1}) + d_{2}J_{1}(k_{s}d_{2})]
\end{cases} \Rightarrow \text{If } d_{1} = 0:$$

$$\begin{cases}
A_{0} = [i\pi Q_{0}/(2k_{s}\mu)]d_{2}H_{1}^{(1)}(k_{s}d_{2}) \\
B_{0} = A_{0} \\
C_{0} = 0 \\
D_{0} = [i\pi Q_{0}/(2k_{s}\mu)]d_{2}J_{1}(k_{s}d_{2})
\end{cases}$$

$$(13)$$

If  $d_1 = 0$ , the shear wave in Eq. (10) is given by:

$$S(r_0; \omega_s) = \begin{cases} B_0 J_0(k_s r_0) - Q_0 / (k_s^2 \mu) = [i\pi Q_0 / (2k_s \mu)] d_2 H_1^{(1)}(k_s d_2) J_0(k_s r_0) - Q_0 / (k_s^2 \mu), & 0 \le r_0 \le d_2 \\ D_0 H_0^{(1)}(k_s r_0) = [i\pi Q_0 / (2k_s \mu)] d_2 J_1(k_s d_2) H_0^{(1)}(k_s r_0), & r_0 > d_2 \end{cases}.$$

$$(14)$$

Eq. (14) is important since it shows that a modulator (focused shear wave) also can be produced using a conventional focused beam (see Figs. 1(c) and 1(d) when  $t_2 < t_1$ ), which may be ignored previously in shear-wave imaging using radiation forces [25][28]. In this case, the same conventional focused transducer can be used to produce both shear wave and imaging wave, which may simplify the imaging systems. Also, because the propagation distance of the shear wave is minimized and thus the effects of shear-wave attenuation is reduced, shear wave of a higher frequency can be used to further increase the image resolution. However, since the focal area of the shear wave overlaps with the area of radiation force  $(-Q_0/(k_s^2\mu))$  in Eq. (14), there may be interference between them, although it is possible to remove such interference in the image reconstructions (see Fig. 1).

From Eq. (13), it is clear that at certain shear-wave frequencies (related to  $k_s$ ) or radii ( $d_1$  and  $d_2$ ) of the cylindrical ring, the coefficients of the shear wave will have peaks (constructive interferences), i.e., the shear wave can resonate, boosting the amplitude of the shear wave  $S(r_0; \omega_s)$  in Eq. (10) and increasing the phase shift to the imaging waves, which will increase the signal-to-noise ratio (SNR) of the super-resolution imaging [15]. Note that a Fabry-Perot type of resonance [29] can be established in a uniform media by a cylindrical ring of radiation force if the force could form a partially reflective boundary of effective stiffness discontinuities caused by localized oscillatory stresses (for simplicity, the effective stiffness discontinuities, if there are any, were not considered in Eq. (10)) to further increase the SNR of super-resolution imaging [15]. To produce a stronger Fabry-Perot resonance, the radiation force can be phase locked with the shear wave it produced through a feedback mechanism [26]. A strong resonance can increase the nonlinear components of the shear wave, which can be used for tissue identification to distinguish between malignant and benign tissues without biopsies in super-resolution imaging.

To reduce sidelobes of super-resolution images, the imaging waves modulated by two shear waves produced at two moments of time,  $t_1$  and  $t_2$ , before and after an interference peak is formed at the ring center can be subtracted, where  $|t_2-t_1|=1/f_s$  should be one shear-wave period, as illustrated in Figs. 1(c) and 1(d), and Fig. 2. Note that the sensitivity and dynamic range, and thus the resolution of super-resolution imaging, can be greatly increased if the modulated imaging waves can interfere coherently before being detected (see the block diagram in lower-left corner of Fig. 1 and P. 167 of Ref. [15]), where the modulators can be either the focused shear waves or small physical particles (such as nanoparticles or may be optically opaque ions for atomic imaging) [15].

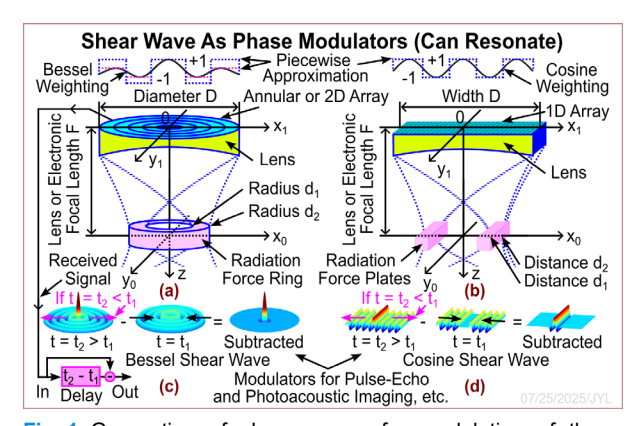


Fig. 1. Generation of shear waves for modulation of the phase of the point spread function (PSF) of an imaging system (such as pulse-echo and photoacoustic [23] imaging) for super-resolution imaging [15]. (a) A focused Bessel beam (or its piecewise or binary approximation) produced by an annular array or a two-dimensional (2D) array transducer is used to generate a cylindrical ring of radiation force at the focal distance (see experiment results in Ref. [30]). (b) A focused cosine beam (or its piecewise or binary approximation) produced by a onedimensional (1D) array transducer is used to obtain two plates of radiation force at the focal distance. (c) A circular low-sidelobe sharp interference peak (right) is produced by subtracting two shear waves generated by an annular or 2D array transducer in (a) at two moments of time  $t_1$  (middle) and  $t_2$  (left) to obtain a net modulation of the imaging wave for low-sidelobe super-resolution imaging of mechanical properties (shear-wave amplitude, speed, spectrum, and nonlinearity) of the object. (d) Same as (c) except that the shear waves are produced by a focused cosine beam with a 1D array transducer in (b). Note that if the pink delay-subtraction unit at the lower-left corner of the figure can be used to interfere coherently for either ultrasound or optical waves modulated by the shear waves obtained in either (a) or (b) before being detected, the sensitivity and dynamic range of the super-resolution imaging system can be greatly increased (Fig. 9 and Page 167 of Ref. [15]). Such an increase in sensitivity may make atomic imaging possible using opaque ions as modulators in an optical imaging system (see the interferometer on Page 167 of Ref. [15]). Also, the shear waves in (c) and (d) may resonate to boost wave amplitude or signal-to-nose ratio (SNR) under certain boundary conditions such as those produced with a phase-locked radiation force [26]. However, in this case, the sidelobes of the cosine shear wave may be high and thus a computerized tomography (CT) method using the resonant cosine shear waves at different azimuthual angles as projections may be needed to reconstruct a super-resolution image. Also note that, in (c) and (d), if  $t_2$  $> t_1$ , the radiation force ring in (a) or plates in (b) are needed to obtain a sharp peak. If  $t_2 < t_1$ , scaling parameter  $\alpha$  in the Bessel and cosine aperture weightings

can be set to zero (i.e., the radius or distance d1 is zero) to produce conventional focused beams for super-resolution imaging. In this case, the effects of shear wave attenuation can be reduced since the shear wave propagation distance is minimized. However, the sidelobes of the subtracted shear waves may be higher because there may be interference between the shear waves ((c) or (d)) and a displacement produced by the radiation force in the focal region of the transducers. To form a super-resolution image, if an annular array in (a) is used, the mechnical scanning system in Figs. 7 and 8 of Ref. [20] can be used. However, if a 2D array in (a) or a 1D array in (b) is used, the beams can be steered electronically to form super-resolution images.

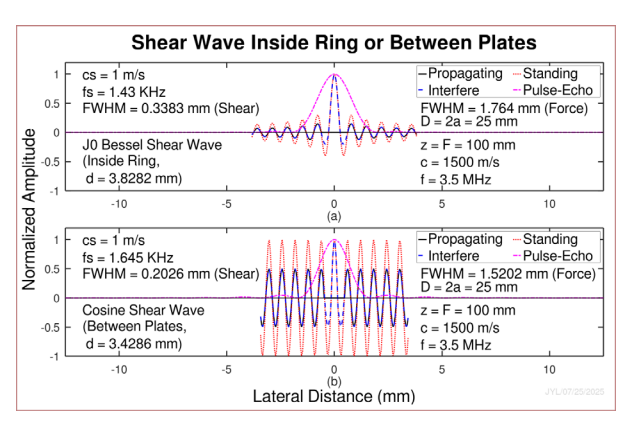


Fig. 2. Shear waves for low-sidelobe super-resolution imaging (also see Figs. 1(c) and 1(d)) (shear waves within and outside of the ring or plates are not included since they are irrelevant, and shear-wave attenuation is not considered). (a) Results obtained with a focused Bessel beam transducer (annular or 2D array in Fig. 1(a)) (b) Results obtained with a focused cosine beam transducer (1D array in Fig. 1(b)). Solid lines (black) are shear waves at a moment of time before an interference peak is formed. Dashed lines (blue) represent shear waves at another moment of time when the interference peak is formed. Dotted lines (red) are standing waves whose peak amplitudes depending on boundary conditions at  $d_1$  and  $d_2$  in Fig. 1 ( $d = (d_1+d_2)/2$  and  $(d_2-d_1)$ = FWHM of the radiation force) and shear-wave frequency. Dash-dotted lines (pink) shows the pulse-echo (two-way) PSF of the imaging system (for photoacoustic imaging, the PSF will be wider since it only has one-way focusing). It is clear that with the parameters given in the figure, super-resolution images can be obtained at a deep depth (z = F = 100 mm).

#### b. Solutions Using Green's Function:

Alternatively, the solutions to Eq. (8) can be obtained with the Green's function method [31]. Assuming that an external line source (along the z direction) is located at (x', y') point in rectangular coordinates or located at the corresponding  $(r', \phi')$  point in cylindrical coordinates, i.e., the line source is given by a Delta function (note that the dimension of a Delta function is an inversion of its argument) [32]:

$$\delta(x_0 - x', y_0 - y') = \delta(x_0 - x')\delta(y_0 - y') = \frac{\delta(r_0 - r')}{r_0}\delta(\phi_0 - \phi') = \frac{\delta(r_0 - r')}{r_0} \left[\frac{1}{2\pi} \sum_{n = -\infty}^{\infty} e^{in(\phi_0 - \phi')}\right],\tag{15}$$

where the periodic function  $\delta(\phi_0 - \phi')$  is expanded as a Fourier series. Replacing the right hand side term of Eq. (8) with Eq. (15) and adding a negative sign, we have:

$$\left(\frac{\partial^{2}}{\partial r_{0}^{2}} + \frac{1}{r_{0}} \frac{\partial}{\partial r_{0}} + \frac{1}{r_{0}^{2}} \frac{\partial^{2}}{\partial \phi_{0}^{2}} + k_{s}^{2}\right) G(r_{0}, r'; \omega_{s}) = -\frac{\delta(r_{0} - r')}{r_{0}} \left[\frac{1}{2\pi} \sum_{n = -\infty}^{\infty} e^{in(\phi_{0} - \phi')}\right], \tag{16}$$

where  $G(r_0, r'; \omega_s)$  is the Green's function of Eq. (8), which is produced by a cylindrical ring source of an infinitely small ring width and an infinitely large amplitude at the ring radius r'. Since the right hand side of Eq. (16) has a dimension of inverse of length squared, in this case,  $G(r_0, r'; \omega_s)$  is dimensionless. Expanding  $G(r_0, r'; \omega_s)$  as a Fourier series in terms of  $\phi_0 - \phi'$ , and then inserting the expansion into Eq. (16), we have:

$$\left(\frac{\partial^{2}}{\partial r_{0}^{2}} + \frac{1}{r_{0}} \frac{\partial}{\partial r_{0}} + \frac{1}{r_{0}^{2}} \frac{\partial^{2}}{\partial \phi_{0}^{2}} + k_{s}^{2}\right) \sum_{n=-\infty}^{\infty} g_{n}(r_{0}, r'; \omega_{s}) e^{in(\phi_{0} - \phi')} = -\frac{\delta(r_{0} - r')}{r_{0}} \left[\frac{1}{2\pi} \sum_{n=-\infty}^{\infty} e^{in(\phi_{0} - \phi')}\right] 
\Rightarrow \left[\frac{d^{2}}{dr_{0}^{2}} + \frac{1}{r_{0}} \frac{d}{dr_{0}} + (k_{s}^{2} - \frac{n^{2}}{r_{0}^{2}})\right] g_{n}(r_{0}, r'; \omega_{s}) = -\frac{\delta(r_{0} - r')}{2\pi r_{0}}; \quad n = -\infty, \dots, -1, 0, 1, \dots, \infty$$
(17)

Setting the right hand side of Eq. (17) to zero, we obtain a homogeneous Helmholtz equation (see Eq. (9)) that can be transformed to an nth-order Bessel equation. Thus, the general solutions to Eq. (17) are given by (see Eq. (10)):

$$g_{n}(r_{0}, r'; \omega_{s}) = g_{n}'(\xi_{0}, \xi'; \omega_{s}) = \begin{cases} A_{n}' J_{n}(k_{s}r_{0}), & r_{0} < r' \\ D_{n}' H_{n}^{(1)}(k_{s}r_{0}), & r_{0} > r' \end{cases}; \quad n = -\infty, \dots, -1, 0, 1, \dots, \infty,$$

$$(18)$$

where  $H_n^{(1)}(k_s r_0) = J_n(k_s r_0) + iY_n(k_s r_0)$  is the nth-order Hankel function of the first kind (outgoing), and  $J_n(k_s r_0)$  and  $Y_n(k_s r_0)$  (Neumann function) are the nth-order Bessel functions of the first and second kind respectively.

Multiplying both sides of Eq. (17) with  $Q(r')/\mu = Q_0/\mu$  and then integrating both sides via r'dr', we obtain a solution to Eq. (8) (since  $S(r_0; \omega_s)$  is independent of  $\phi_0$ , thus n = 0 and the summation over n can be removed):

$$\int_{d_{1}}^{d_{2}} \left\{ \frac{Q(r')}{\mu} \left[ \frac{d^{2}}{dr_{0}^{2}} + \frac{1}{r_{0}} \frac{d}{dr_{0}} + (k_{s}^{2} - \frac{n^{2}}{r_{0}^{2}}) \right] \sum_{n=-\infty}^{\infty} g_{n}(r_{0}, r'; \omega_{s}) e^{in(\phi_{0} - \phi')} \right\} r' dr' = -\int_{d_{1}}^{d_{2}} \left[ \frac{Q(r')}{\mu} \frac{\delta(r_{0} - r')}{r_{0}} \right] \left[ \frac{1}{2\pi} \sum_{n=-\infty}^{\infty} e^{in(\phi_{0} - \phi')} \right] r' dr' \\
\Rightarrow \left[ \frac{d^{2}}{dr_{0}^{2}} + \frac{1}{r_{0}} \frac{d}{dr_{0}} + (k_{s}^{2} - \frac{n^{2}}{r_{0}^{2}}) \right] \left[ \sum_{n=-\infty}^{\infty} \int_{d_{1}}^{d_{2}} \frac{Q(r')}{\mu} g_{n}(r_{0}, r'; \omega_{s}) e^{in(\phi_{0} - \phi')} r' dr' \right] = -\frac{Q(r_{0})}{2\pi\mu} \sum_{n=-\infty}^{\infty} e^{in(\phi_{0} - \phi')} \\
\Rightarrow \left( \frac{d^{2}}{dr_{0}^{2}} + \frac{1}{r_{0}} \frac{d}{dr_{0}} + k_{s}^{2} \right) \left[ 2\pi \int_{d_{1}}^{d_{2}} \frac{Q(r')}{\mu} g_{0}(r_{0}, r'; \omega_{s}) r' dr' \right] = -\frac{Q(r_{0})}{\mu}; \quad \text{(when } n = 0)$$

$$\Rightarrow S(r_{0}; \omega_{s}) = 2\pi \int_{d_{1}}^{d_{2}} \frac{Q(r')}{\mu} g_{0}(r_{0}, r'; \omega_{s}) r' dr' = 2\pi \int_{d_{1}}^{d_{2}} \frac{Q(r')}{\mu} G(r_{0}, r'; \omega_{s}) r' dr'; \quad \text{(when } n = 0)$$

where the Green's function  $G(r_0, r'; \omega_s) = g_0(r_0, r'; \omega_s)$  since n = 0 (see Eq. (16)).

Now let us find the coefficients  $A_n$ ' and  $D_n$ ' for the Green's function in Eq. (18) when n = 0. Applying the continuity boundary condition for  $G(r_0, r'; \omega_s)$  at r', we have:

$$A_0 'J_0(k_s r_0)|_{r_s=r'} = D_0 'H_0^{(1)}(k_s r_0)|_{r_s=r'} \Rightarrow A_0 'J_0(k_s r') - D_0 'H_0^{(1)}(k_s r') = 0.$$
 (20)

Integrating Eq. (17) (n = 0) across the boundary r' and then taking a limit via a real number  $\sigma \to 0$  (another boundary condition with derivative of  $G(r_0, r'; \omega_s)$  and a jump at r'), we obtain another equation for  $A_n$ ' and  $D_n$ ':

$$\lim_{\sigma \to 0} \int_{r^{-}\sigma}^{r^{+}\sigma} \left\{ \frac{1}{r_{0}} \frac{d}{dr_{0}} \left[ r_{0} \frac{dg_{n}(r_{0}, r^{+}; \omega_{s})}{dr_{0}} \right] + \left( k_{s}^{2} - \frac{n^{2}}{r_{0}^{2}} \right) g_{n}(r_{0}, r^{+}; \omega_{s}) \right\} r_{0} dr_{0} = \int_{r^{+}\sigma}^{r^{+}\sigma} \left[ -\frac{\delta(r_{0} - r^{+})}{2\pi r_{0}} \right] r_{0} dr_{0}$$

$$\Rightarrow \lim_{\sigma \to 0} \left[ r_{0} \frac{dg_{n}(r_{0}, r^{+}; \omega_{s})}{dr_{0}} \right] \Big|_{r^{+}\sigma}^{r^{+}\sigma} + \lim_{\sigma \to 0} \int_{r^{+}\sigma}^{r^{+}\sigma} \left[ \left( k_{s}^{2} - \frac{n^{2}}{r_{0}^{2}} \right) g_{n}(r_{0}, r^{+}; \omega_{s}) \right] r_{0} dr_{0} \right\} = -\frac{1}{2\pi}; \quad \text{(Note: the second lim is 0 due to Eq. (20))}$$

$$\Rightarrow \lim_{\sigma \to 0} \left\{ D_{n} \frac{d[H_{n}^{(1)}(k_{s}r_{0})]}{dr_{0}} \Big|_{r^{+}\sigma} - A_{n} \frac{d[J_{n}(k_{s}r_{0})]}{dr_{0}} \Big|_{r^{+}\sigma} \right\} = -\frac{1}{2\pi r^{+}}$$

$$\Rightarrow -A_{n} \left[ J_{n-1}(k_{s}r^{+}) - J_{n+1}(k_{s}r^{+}) \right] / 2 + D_{n} \left[ H_{n-1}^{(1)}(k_{s}r^{+}) - H_{n+1}^{(1)}(k_{s}r^{+}) \right] / 2 = -1/(2\pi k_{s}r^{+}); \quad n = -\infty, \dots, -1, 0, 1, \dots, \infty$$

$$\Rightarrow A_{0} \left[ J_{1}(k_{s}r^{+}) - D_{0} \left[ H_{1}^{(1)}(k_{s}r^{+}) \right] - 1/(2\pi k_{s}r^{+}); \quad \text{(when } n = 0) \right]$$

Combining Eqs. (20) and (21) and then writing them in a matrix form, we have:

$$\begin{cases}
A_0' J_0(k_s r') - D_0' H_0^{(1)}(k_s r') = 0 \\
A_0' J_1(k_s r') - D_0' H_1^{(1)}(k_s r') = -1/(2\pi k_s r')
\end{cases} \Rightarrow \mathbf{A}\mathbf{x} = \mathbf{b} \Rightarrow \mathbf{A} = \begin{bmatrix} J_0(k_s r') & -H_0^{(1)}(k_s r') \\ J_1(k_s r') & -H_1^{(1)}(k_s r') \end{bmatrix}, \mathbf{x} = \begin{bmatrix} A_m' \\ D_m' \end{bmatrix}, \mathbf{b} = \begin{bmatrix} 0 \\ -1/(2\pi k_s r') \end{bmatrix}. (22)$$

Solving Eq. (22), we get the coefficients:

$$\Delta = |\mathbf{A}| = H_0^{(1)}(k_s r') J_1(k_s r') - J_0(k_s r') H_1^{(1)}(k_s r') = 2i/(\pi k_s r')$$

$$\Delta_{1} = |\mathbf{A}_{1}| = \begin{vmatrix} 0 & -H_{0}^{(1)}(k_{s}r') \\ -1/(2\pi k_{s}r') & H_{1}^{(1)}(k_{s}r') \end{vmatrix} = -\frac{H_{0}^{(1)}(k_{s}r')}{2\pi k_{s}r'}; \quad \Delta_{2} = |\mathbf{A}_{2}| = \begin{vmatrix} J_{0}(k_{s}r') & 0 \\ J_{1}(k_{s}r') & -1/(2\pi k_{s}r') \end{vmatrix} = -\frac{J_{0}(k_{s}r')}{2\pi k_{s}r'}.$$

$$A_{0}' = \Delta_{1}/\Delta = -[1/(2\pi k_{s}r')]H_{0}^{(1)}(k_{s}r')/\Delta = -[1/(2\pi k_{s}r')]H_{0}^{(1)}(k_{s}r')/[2i/(\pi k_{s}r')] = (i/4)H_{0}^{(1)}(k_{s}r')$$

$$D_{0}' = \Delta_{2}/\Delta = -[1/(2\pi k_{s}r')]J_{0}(k_{s}r')/\Delta = -[1/(2\pi k_{s}r')]J_{0}(k_{s}r')/[2i/(\pi k_{s}r')] = (i/4)J_{0}(k_{s}r')$$
(23)

From Eqs. (18), (19), and (23), the final solution is given by:

$$S(r_{0};\omega_{s}) = 2\pi \int_{d_{1}}^{d_{2}} \frac{Q(r')}{\mu} G(r_{0},r';\omega_{s})r'dr' = \begin{cases} \frac{i\pi}{2\mu} \left[ \int_{d_{1}}^{d_{2}} Q_{0}H_{0}^{(1)}(k_{s}r')r'dr' \right] J_{0}(k_{s}r_{0}), & r_{0} < d_{1} \\ \frac{i\pi}{2\mu} \left\{ \left[ \int_{d_{1}}^{r_{0}} Q_{0}J_{0}(k_{s}r')r'dr' \right] H_{0}^{(1)}(k_{s}r_{0}) + \left[ \int_{r_{0}}^{d_{2}} Q_{0}H_{0}^{(1)}(k_{s}r')r'dr' \right] J_{0}(k_{s}r_{0}) \right\}, & d_{1} \leq r_{0} \leq d_{2} . (24) \\ \frac{i\pi}{2\mu} \left[ \int_{d_{1}}^{d_{2}} Q_{0}J_{0}(k_{s}r')r'dr' \right] H_{0}^{(1)}(k_{s}r_{0}), & r_{0} > d_{2} \end{cases}$$

It can be proved that Eq. (24) is exactly the same as Eq. (10) since  $\int H_0^{(1)}(x)xdx = xH_1^{(1)}(x)$  and  $\int J_0(x)xdx = xJ_1(x)$ . Thus, there will be resonant peaks or constructive interference at certain  $k_s$  and dimensions of the ring as mentioned above. However, unlike Eq. (10), Eq. (24) is more general since Q(r') in Eq. (8) can be any well-behaved function within the ring  $0 < d_1 \le r_0 \le d_2$ , which is the case for a remotely generated radiation force, although more computations are needed for the integrations in Eq. (24) if Q(r') is not a constant.

#### c. Resonance Gain:

The shear wave in free space (no resonance) can be obtained by getting a particular solution to Eq. (8) but without the boundaries at  $d_1$  and  $d_2$  (i.e.,  $Q(r_0) \equiv Q_0$  for all  $r_0$ ):

$$S_{ref}(r_0; \omega_s) = -Q_0/(k_s^2 \mu)$$
, (25)

where the subscript "ref" means "reference". The resonance gain of the shear wave at  $r_0 = 0$  is given by [33]:

$$E(k_s) = \left| \frac{S(r_0; \omega_s)}{S_{ref}(r_0; \omega_s)} \right|_{r_0 = 0} = \left| \frac{A_0 J_0(k_s r_0)}{S_{ref}(r_0; \omega_s)} \right|_{r_0 = 0} = \left| \frac{A_0}{-Q_0 / (k_s^2 \mu)} \right| = \frac{k_s^2 \mu}{Q_0} |A_0|,$$
(26)

which is a ratio between the amplitude of the shear wave (see Eqs. (10) and (13)) produced by a cylindrical ring of external force and the amplitude of the reference shear wave in Eq. (25) at the center of the ring.

Fig. 3(a) shows a plot of  $E(k_s)$  versus the shear-wave frequency  $f_s = k_s c_s / (2\pi)$ . It is clear that shear wave resonates at specific frequencies and the peak of the resonance gain increases with the frequency. From Eqs. (13)

and (26), it can be shown that  $E(k_s)$  also increases with the size of the ring  $(d = (d_1 + d_2)/2)$  and the number of peaks of  $E(k_s)$  is reduced as the ring width  $d_2 - d_1$  decreases.

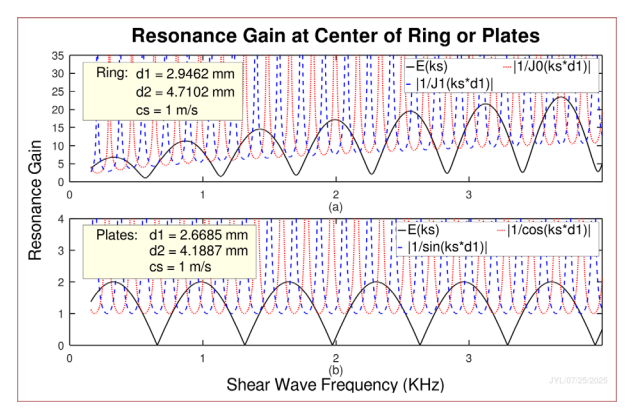


Fig. 3. Theoretical resonance gains of shear waves over frequency without attenuation. (a) Resonance gain of the

shear wave produced by a cylindrical ring of radiation force (see Fig. 1(a)). (b) Resonance gain of the shear wave produced by two plates of radiation force (see Fig. 1(b)). Solid lines (black) represent the results of the continuity boundary conditions at both  $d_1$  and  $d_2$  (see Fig. 1). Dotted (red) and dashed (blue) lines are resonance gains of the shear waves produced with a constant amplitude and shear stress at the boundary  $d_1$  respectively. In these cases, the resonance gain at some frequencies can be infinity. A large resonance gain increases the SNR of imaging systems. The parameters used are given in the figure.

#### d. Radiation Force of Longitudinal Wave Produced by a Focused Bessel Beam at Its Focus:

If  $r_0 \ll a$  (paraxial condition), the ultrasound longitudinal-wave pressure produced by a focused transducer (radius a) weighted with an nth-order Bessel function  $J_n(\alpha r_1)$ , where  $\alpha \ge 0$  is the scaling parameter and  $r_1 = \sqrt{x_1^2 + y_1^2}$  is the radial distance of a point  $(x_1, y_1)$  on the transducer aperture, is given by (see Eqs. (31) and (32) of Ref. [21], P. 943 of Ref. [34], and P. 661 of Ref. [35]):

$$\tilde{\Phi}_{B_n}(x_0, y_0, z = F; \omega) = \frac{e^{ikF}}{i\lambda F} (1 + \frac{i\lambda}{2\pi F}) e^{i\frac{k}{2F}r_0^2} (2\pi i^{-n} e^{in\phi}) \Im_n \{J_n(\alpha r_1)\}(k_0),$$
(27)

where the subscript " $B_n$ " means nth-order Bessel beam, n is an integer, F is a focal distance,  $\omega = 2\pi f$  is an angular frequency, f is the frequency,  $k = \omega/c = 2\pi/\lambda$  is the wavenumber,  $\lambda$  is the wavelength, c is the speed of sound,  $k_0 = kr_0/F$ ,  $r_0$  is the radial distance from the beam axis at the focal distance,  $\phi$  is an azimuthal angle, and  $\mathcal{H}_n\{J_n(\alpha r_1)\}(k_0)$  is a Hankel transform of  $J_n(\alpha r_1)$ : (see Eq. (32) of Ref. [21], P. 619 of Ref. [34], and P. 664 of Ref. [35]):

$$\Re_{n} \{J_{n}(\alpha r_{1})\}(k_{0}) = \int_{0}^{a} \{J_{n}(\alpha r_{1})\}J_{n}(k_{0}r_{1})r_{1}dr_{1} = \begin{cases}
a^{2} \frac{(\alpha a)J_{n}(k_{0}a)J_{n+1}(\alpha a) - (k_{0}a)J_{n}(\alpha a)J_{n+1}(k_{0}a)}{(\alpha a)^{2} - (k_{0}a)^{2}}, & k_{0} \neq \alpha \\
(\alpha a)^{2} - (k_{0}a)^{2} & . \\
a^{2} \frac{(\alpha a)[J_{n}^{2}(\alpha a) + J_{n+1}^{2}(\alpha a)] - 2nJ_{n}(\alpha a)J_{n+1}(\alpha a)}{2(\alpha a)}, & k_{0} = \alpha
\end{cases}$$
(28)

At  $k_0 = \alpha$ , there is a peak in Eq. (28) (see Figs. 4 and 5), which means that the sound pressure produced by a focused Bessel transducer is a cylindrical ring of a radius of  $r_0 = \alpha F/k$  and the ring thickness becomes zero as  $a \to \infty$  (see Eqs. (31) and (32) of Ref. [21]). If n = 0, Eq. (28) becomes:

$$\Re_{0} \{J_{0}(\alpha r_{1})\}(k_{0}) = \begin{cases}
a^{2} \frac{(\alpha a)J_{0}(k_{0}a)J_{1}(\alpha a) - (k_{0}a)J_{0}(\alpha a)J_{1}(k_{0}a)}{(\alpha a)^{2} - (k_{0}a)^{2}}, & k_{0} \neq \alpha \\
a^{2} \frac{J_{0}^{2}(\alpha a) + J_{1}^{2}(\alpha a)}{2}, & k_{0} = \alpha \\
a^{2} \frac{1}{2} \operatorname{Jinc}(\alpha a), & k_{0} = 0 \\
\approx a^{2} \frac{J_{0}(\alpha a)}{2} \left[\frac{2J_{1}(k_{0}a)}{(k_{0}a)}\right] = a^{2} \frac{J_{0}(\alpha a)}{2} \operatorname{Jinc}(k_{0}a), & k_{0} \gg \alpha \text{ and } J_{0}(\alpha a) \neq 0
\end{cases} (29)$$

From Eq. (29), it is clear that the asymptotic behavior ( $k_0 \gg \alpha$  and  $k_0 = 0$ ) of the sound pressure in Eq. (27) from the peak pressure on the ring is similar to a Jinc function (defined as  $Jinc(x) = 2J_1(x)/x$ ), which is similar to the

beam profile of a focused plane wave produced by a disk transducer of a radius a. I.e., if  $\alpha = 0$  in Eqs. (27) and (29), we have (see Eqs. (35) and (36) of Ref. [21], and Eqs. 2-35 and 4-31 of Ref. [31]):

$$\tilde{\Phi}_{P}(x_{0}, y_{0}, z = F; \omega) = \frac{e^{ikF}}{i\lambda F} (1 + \frac{i\lambda}{2\pi F}) e^{i\frac{k}{2F}r_{0}^{2}} [\pi a^{2} \operatorname{Jinc}(k_{0}a)], \qquad (30)$$

where the subscript "P" means "plane wave". At  $k_0 = 0$ , i.e., at the center of the ring  $r_0 = 0$ , Eq. (29) is given by  $(a^2/2) \text{Jinc}(\alpha a)$ . Thus, to produce a ring of radiation force where the sound pressure is 0 at  $r_0 = 0$ , which is desired,  $\alpha a$  should be chosen so that  $\text{Jinc}(\alpha a)$  (or  $J_1(\alpha a)$ ) is zero, i.e.,  $\alpha = 3.8317/a$ , 7.0156/a, 10.1735/a, 13.3237/a, and 16.4706/a, etc.

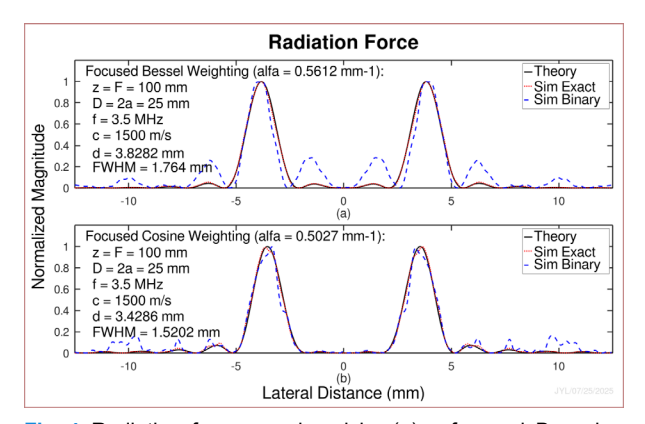


Fig. 4. Radiation forces produced by (a) a focused Bessel beam transducer (see Fig. 1(a)) and (b) a cosine beam transducer (see Fig. 1(b)). Solid lines (black) were obtained theoretically with the Rayleigh-Sommerfeld diffraction formula. Dotted lines (red) are the results of computer simulations with an exact Bessel or cosine aperture weighting. Dashed lines (blue) are the same as dotted lines except that a piecewise (binary) aperture weighting was used to increase transmit power. The parameters used are shown in the figure. An experiment result of the radiation force using a focused Bessel beam can be found in [30].

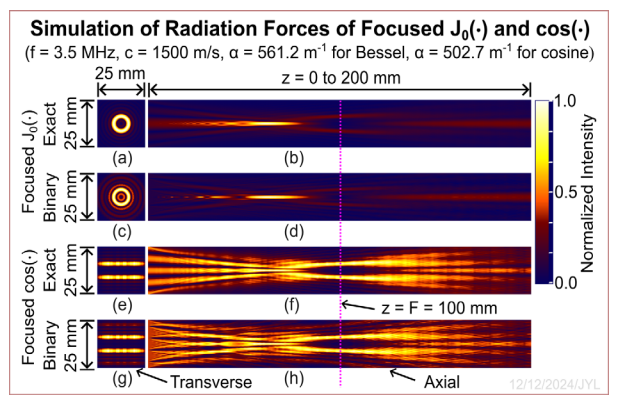


Fig. 5. Simulated radiation forces of the same parameters as those used in Fig. 4. (a) and (b) are transverse (x-y plane at z = 100 mm, see the vertical pink line) and axial (x-z plane from z = 0 to 200 mm) profiles, respectively, of the radiation force produced by a focused Bessel transducer (see Fig. 1(a)) with an exact aperture weighting. (c) and (d) are the same as (a) and (b) respectively except that a piecewise (binary) aperture weighting is used to increase transmit power. (e) to (h) are the same as (a) to (d) respectively except that a focused cosine transducer (see Fig. 1(b)) is used. The color bar shows normalized beam intensity or radiation force.

Using Eqs. (27)-(29), the radiation force, i.e., the body force  $Q(r_0)$  in Eq. (8) or Eq. (24) on the cylindrical ring can be calculated since the radiation force is proportional to the intensity or the square of the magnitude of the sound pressure,  $|\tilde{\Phi}_{B_n}(x_0, y_0, z = F; \omega)|^2$ . Thus, the full-width-at-half-maximum (FWHM) width of the cylindrical ring of the body force is determined by the square of the Jinc function in Eq. (29), i.e.,  $PR_{FWHM}^2 = 2r_0 \approx 1.029\lambda F/D$ , as explained in the paragraph below Eq. (37) of Ref. [21] since  $\text{Jinc}^2(1.61633) = 0.5$  and thus  $r_0 = 1.61633F/(ka) = (1.61633/\pi)\lambda F/D$ , where D = 2a is the diameter of the transducer.  $R_{FWHM}$  in  $PR_{FWHM}^2$  means the FWHM resolution, the superscript "2" means "squared", and the prefix P means focused "plane wave".

Assuming F=100 mm, D=25 mm, f=3.5 MHz, and c=1500 m/s, then  $\lambda=c/f=0.4286$  mm and  $PR_{FWHM}^2=1.764$  mm. If we choose the radius of the ring corresponding to one of the zeros (such as the second zero) of the  $J_1(\alpha a)$  function,  $d=\alpha F/k=7.0156F/(ka)=3.8282$  mm, we obtain  $d_1=d-(PR_{FWHM}^2/2)=2.9462$  mm and  $d_2=d+(PR_{FWHM}^2/2)=4.7102$  mm for Eq. (10). To produce a ring of radius d, the scaling parameter of the Bessel beam should be  $\alpha=7.0156/a=kd/F=0.5612$  mm<sup>-1</sup>. Given these parameters, a line plot of the radiation force through the diameter of the ring is give in Fig. 4(a) with n=0 (Figs. 5(a) to 5(d) are the corresponding cross sections of the radiation force). To increase the total transmission energy and thus increase the radiation force on the cylindrical ring, both a smaller ring radius and a piecewise (binary) focused Bessel aperture weighting can be used [19], i.e., setting  $J_0(\alpha r_1)=1$  if  $J_0(\alpha r_1)\geq 0$ , and  $J_0(\alpha r_1)=-1$  otherwise.

#### II. FIXED SHEAR WAVE APPLITUDE OR STRESS AT THE CYLINDRICAL RING BOUNDARY

Assuming that a cylindrical ring has a radius  $d_1 > 0$  and is vibrating uniformly along z axis at a single frequency with a fixed amplitude A. According to Eq. (10), the shear wave produced inside the ring is given by:

$$S(r_0; \omega_s) = A_0 " J_0(k_s r_0); \text{ where } 0 \le r_0 < d_1,$$
 (31)

where  $A_0$  is a coefficient to be determined with the continuity boundary condition (i.e.,  $S(r_0; \omega_s) = A$  at  $d_1$ ):

$$A_0"J_0(k_sd_1) = A \Rightarrow A_0" = \frac{A}{J_0(k_sd_1)} \Rightarrow S(r_0;\omega_s) = \frac{A}{J_0(k_sd_1)} J_0(k_sr_0).$$
(32)

In this case, it is easy to see that the shear wave produced inside the ring can have Fabry-Perot-type resonances [29], i.e.,  $S(r_0; \omega_s) \to \infty$  as  $J_0(k_s d_1) \to 0$  (or when  $k_s d_1 \to 2.4048$ , 5.5201, 8.6537, 11.7915, and 14.9309, etc) at certain shear-wave frequencies or ring radii, and the resonance gain (normalized to A) in Eq. (26) will be infinity if there is no shear-wave attenuation (see red dotted line in Fig. 3(a)). Thus, if such a boundary condition could be realized via methods such as phase-locked radiation force [26], a large resonance gain ( $|1/J_0(k_s d_1)|$ ) could be produced for studying the nonlinear properties of objects such as biological soft tissues.

If at the boundary  $d_1$ , a harmonic shear stress is uniformly applied along the z axis with a fixed amplitude  $T_{d_1}$  ( $N/m^2$ ), using Eq. (10), the boundary condition and the resulting shear wave inside the ring is given by:

$$\mu \frac{dS(r_0; \omega_s)}{dr_0} \Big|_{r_0 = d_1} = T_{d_1} \Rightarrow \mu[-A_0 k_s J_1(k_s d_1)] = T_{d_1} \Rightarrow A_0 = -\frac{T_{d_1}}{\mu k_s J_1(k_s d_1)} \Rightarrow S(r_0; \omega_s) = -\frac{T_{d_1}}{\mu k_s J_1(k_s d_1)} J_0(k_s r_0). \tag{33}$$

In this case, the shear wave inside the cylindrical ring will resonate as  $J_1(k_sd_1) \rightarrow 0$  (or when  $k_sd_1 \rightarrow 0$ , 3.8317, 7.0156, 10.1735, and 13.3237, etc). I.e., the resonance gain (normalized to  $-T_{d_1}/(\mu k_s)$ ) will be  $|1/J_1(k_sd_1)|$  (see blue dashed line in Fig. 3(a)). The boundary conditions in Eqs. (32) and (33) can be realized by controlling how the force is applied remotely or locally in various applications such as NDE.

#### III. SHEAR WAVE PRODUCTION WITH TWO PARALLEL PLATES OF RADIATION FORCE

#### a. Solutions to the Wave Equation:

If the cylindrical ring in Fig. 1(a) is replaced with two infinitely large parallel plates located symmetrically about  $x_0 = 0$  (see Fig. 1(b)), Eq. (6) becomes a one-dimensional (1D) equation that can be used for a 1D array transducer commonly used in medical ultrasound imaging systems:

$$\left[\frac{\partial^2}{\partial x_0^2} - \frac{1}{c_s^2(x_0;t)} \frac{\partial^2}{\partial t^2}\right] \vec{s}(x_0;t) = -\frac{\vec{q}(x_0;t)}{\mu}.$$
 (34)

Assuming that  $\vec{s}(x_0;t) = s(x_0;t)\vec{z}^0 = S(x_0;\omega_s)e^{-i\omega_s t}\vec{z}^0$ ,  $\vec{q}(x_0;t) = q(x_0;t)\vec{z}^0 = Q(x_0)e^{-i\omega_s t}\vec{z}^0$ ,  $c_s(x_0;t) = c_s$  is a constant,  $k_s = \omega_s / c_s$ , where  $Q(x_0) = Q_0$  is a constant for  $0 < d_1 \le |x_0| \le d_2$ , and  $Q(x_0) = 0$  elsewhere, Eq. (8) becomes a 1D Helmholtz equation:

$$\frac{d^2S(x_0; \omega_s)}{dx_0^2} + k_s^2 S(x_0; \omega_s) = \begin{cases} -\frac{Q_0}{\mu}, & 0 < d_1 \le |x_0| \le d_2 \\ 0, & \text{Otherwise} \end{cases}$$
 (35)

Similar to Eq. (10), the solutions to Eq. (35) can be obtained using a general solution to the homogeneous Helmholtz equation plus a specific solution to the inhomogeneous Helmholtz equation:

$$S(x_0; \omega_s) = \begin{cases} (A_0 \text{ "}/2)e^{ik_s x_0} + (A_0 \text{ "}/2)e^{-ik_s x_0} = A_0 \text{ "}\cos(k_s x_0), & -d_1 < x_0 < d_1 \\ B_0 \text{ "}e^{ik_s x_0} + C_0 \text{ "}e^{-ik_s x_0} - Q_0 / (k_s^2 \mu), & 0 \le d_1 \le x_0 \le d_2 \text{ or } -d_2 \le x_0 \le -d_1 . \\ D_0 \text{ "}e^{ik_s x_0}, & x_0 \le -d_2 \text{ or } x_0 > d_2 \end{cases}$$
 (36)

Note that similar to cylindrical ring, the shear wave produced will propagate towards the axis of the transducer in Fig. 1(b) to form a standing wave given in Eq. (36). During the propagation, the imaging waves can be modulated at two moments of time as in Figs. 1(d) and Figs. 2(b) for low-sidelobe and high-contrast super-resolution imaging.

Applying the boundary conditions of continuity of displacement and stress to Eq. (36), we have:

$$\begin{cases} (1) \text{ At } x_0 = d_1 \text{ (Displacement Continuity):} & A_0 \text{```cos}(k_s d_1) = B_0 \text{``'}e^{ik_s d_1} + C_0 \text{``'}e^{-ik_s d_1} - Q_0 / (k_s^2 \mu) \\ (2) \text{ At } x_0 = d_1 \text{ (Stress Continuity):} & d[A_0 \text{``cos}(k_s x_0)] / dx_0 \mid_{x_0 = d_1} = d[B_0 \text{``'}e^{ik_s x_0} + C_0 \text{``'}e^{-ik_s x_0}] / dx_0 \mid_{x_0 = d_1} \\ (3) \text{ At } x_0 = d_2 \text{ (Displacement Continuity):} & B_0 \text{```}e^{ik_s d_2} + C_0 \text{```}e^{-ik_s d_2} - Q_0 / (k_s^2 \mu) = D_0 \text{```}e^{ik_s d_2} \\ (4) \text{ At } x_0 = d_2 \text{ (Stress Continuity):} & d[B_0 \text{```}e^{ik_s x_0}] / dx_0 \mid_{x_0 = d_2} = d[D_0 \text{```}e^{ik_s x_0}] / dx_0 \mid_{x_0 = d_2} \\ \Rightarrow (1) A_0 \text{```cos}(k_s d_1) - B_0 \text{```}e^{ik_s d_1} - C_0 \text{```}e^{-ik_s d_1} = -Q_0 / (k_s^2 \mu); & (2) - A_0 \text{```sin}(k_s d_1) - iB_0 \text{```}e^{ik_s d_1} + iC_0 \text{```}e^{-ik_s d_1} = 0; \\ (37) \text{ (3)} B_0 \text{```}e^{ik_s d_2} + C_0 \text{```}e^{-ik_s d_2} - D_0 \text{```}e^{ik_s d_2} = Q_0 / (k_s^2 \mu); & (4) B_0 \text{```}e^{ik_s d_2} - C_0 \text{```}e^{-ik_s d_2} - D_0 \text{```}e^{ik_s d_2} = 0 \end{cases}$$

Solving Eq. (37), we obtain the coefficients  $A_0$  ",  $B_0$  ",  $C_0$  ", and  $D_0$  " of the shear wave in Eq. (36):

$$A_0 = [Q_0/(2k_s^2\mu)](2e^{ik_sd_2} - 2e^{ik_sd_1}); \quad B_0 = [Q_0/(2k_s^2\mu)][-2i\sin(k_sd_1) + e^{ik_sd_2}]$$

$$C_0 = [Q_0/(2k_s^2\mu)]e^{ik_sd_2}; \quad D_0 = [Q_0/(2k_s^2\mu)][2i\sin(k_sd_2) - 2i\sin(k_sd_1)]$$
(38)

From Eq. (38), it is seen that at certain shear-wave frequencies (related to  $k_s$ ) or plate positions ( $d_1$  and  $d_2$ ), the coefficients of the shear wave will have peaks (resonance) or zeros (anti-resonance). However, unlike the shear wave in a cylindrical ring, the maximum resonance gain (normalized to  $-Q_0/(k_s^2\mu)$ ) at the center of the two plates at  $x_0 = 0$  is 2 and it does not increase as the shear wave frequency increases (see the black solid line in Fig. 3(b)).

As mentioned before, if a Fabry-Perot type of resonance can be established, as in Eq. (32) or (33), the resonance gain can be very large which increases the SNR. I.e., if at the boundary  $d_1$ , the shear wave amplitude A is a constant, the resonance gain (normalized to A) will be  $|1/\cos(k_s d_1)|$  (see red dotted line in Fig. 3(b)). If a harmonic shear stress of a constant amplitude  $T_{d_1}$  is applied at the boundary, the resonance gain (normalized to  $-T_{d_1}/(\mu k_s)$ ) will be  $|1/\sin(k_s d_1)|$  (see blue dashed line in Fig. 3(b)). Note that the constant displacement A or shear stress  $T_{d_1}$  at the boundary  $d_1$  can be realized by controlling the force applied remotely or locally in various applications including NDE.

#### b. Radiation Force of Longitudinal Wave Produced by a Focused Cosine Beam at Its Focus:

The longitudinal ultrasound wave pressure at the focal distance F of a focused beam produced by a transducer located at the plane z=0 in rectangular coordinates is given by (see Eq. (28) of Ref. [21]) (Eq. 5-14 of Ref. [31]):

where  $k_{x_0} = kx_0/F$  and  $k_{y_0} = ky_0/F$ , and  $\tilde{\Phi}'_1(x_1, y_1; \omega)$  is the weighting function at the transducer aperture on the coordinates  $(x_1, y_1)$  before a physical lens or an electronic focusing is applied. If the transducer is one-dimensional (uniform over the elevation dimension in  $y_1$ ) and is weighted with a cosine function  $\cos(\alpha x_1)$ , where  $\alpha \ge 0$  is the scaling parameter, the ultrasound beam at the focal distance is given by the following 1D Fourier transform:

$$\tilde{\Phi}(x_{0}, z = F; \omega) = \frac{e^{ikF}}{i\lambda F} (1 + \frac{i\lambda}{2\pi F}) e^{i\frac{k}{2F}x_{0}^{2}} \int_{-a}^{a} \cos(\alpha x_{1}) e^{-ik_{x_{0}}x_{1}} dx_{1} = \frac{e^{ikF}}{i\lambda F} (1 + \frac{i\lambda}{2\pi F}) e^{i\frac{k}{2F}x_{0}^{2}} \int_{-a}^{a} \frac{e^{i\alpha x_{1}} + e^{-i\alpha x_{1}}}{2} e^{-ik_{x_{0}}x_{1}} dx_{1}$$

$$= \frac{e^{ikF}}{i\lambda F} (1 + \frac{i\lambda}{2\pi F}) e^{i\frac{k}{2F}x_{0}^{2}} \begin{cases} \frac{(k_{x_{0}} + \alpha)\sin[(k_{x_{0}} - \alpha)a] + (k_{x_{0}} - \alpha)\sin[(k_{x_{0}} + \alpha)a]}{k_{x_{0}}^{2} - \alpha^{2}} = a\{\sin[(k_{x_{0}} - \alpha)a] + \sin[(k_{x_{0}} + \alpha)a]\}, & k_{x_{0}} \neq \alpha \end{cases}$$

$$= \frac{e^{ikF}}{i\lambda F} (1 + \frac{i\lambda}{2\pi F}) e^{i\frac{k}{2F}x_{0}^{2}} \begin{cases} \frac{(k_{x_{0}} + \alpha)\sin[(k_{x_{0}} - \alpha)\sin[(k_{x_{0}} - \alpha)a] + \sin[(k_{x_{0}} + \alpha)a]\}, & k_{x_{0}} \neq \alpha \end{cases}$$

$$= \frac{e^{ikF}}{i\lambda F} (1 + \frac{i\lambda}{2\pi F}) e^{i\frac{k}{2F}x_{0}^{2}} \begin{cases} \frac{(k_{x_{0}} + \alpha)\sin[(k_{x_{0}} - \alpha)\sin[(k_{x_{0}} - \alpha)a] + \sin[(k_{x_{0}} - \alpha)a] + \sin[(k_{x_{0}} + \alpha)a]\}, & k_{x_{0}} \neq \alpha \end{cases}$$

$$= \frac{e^{ikF}}{i\lambda F} (1 + \frac{i\lambda}{2\pi F}) e^{i\frac{k}{2F}x_{0}^{2}} \begin{cases} \frac{(k_{x_{0}} + \alpha)\sin[(k_{x_{0}} - \alpha)a] + \sin[(k_{x_{0}} - \alpha)a] + \sin[(k_{x_{0}} - \alpha)a] + \sin[(k_{x_{0}} - \alpha)a]\}, & k_{x_{0}} \neq \alpha \end{cases}$$

$$= \frac{e^{ikF}}{i\lambda F} (1 + \frac{i\lambda}{2\pi F}) e^{i\frac{k}{2F}x_{0}^{2}} \begin{cases} \frac{(k_{x_{0}} + \alpha)\sin[(k_{x_{0}} - \alpha)a] + \sin[(k_{x_{0}} - \alpha$$

where a is the half width of the transducer along the  $x_1$  direction and  $\mathrm{sinc}(x) = \sin(x)/x$  is the sinc function. Eq. (40) has two peaks at  $k_{x_0} = \pm \alpha$  or  $x_0 = \pm F\alpha/k$ , which are symmetric about the  $x_0 = 0$ . To ensure that the ultrasound pressure is zero at  $k_{x_0} = 0$ , from Eq. (40), one should choose  $\mathrm{sinc}(\alpha a) = 0$  (or,  $\alpha = n\pi/a$  where  $n = 1, 2, 3, \cdots$ ). If  $\alpha = 0$ , we obtain focused plane wave at the focal distance of a 1D array transducer:

$$\tilde{\Phi}(x_0, z = F; \omega) = \frac{e^{ikF}}{i\lambda F} (1 + \frac{i\lambda}{2\pi F}) e^{i\frac{k}{2F}x_0^2} \int_{-a}^{a} e^{-ik_{x_0}x_1} dx_1 = \frac{e^{ikF}}{i\lambda F} (1 + \frac{i\lambda}{2\pi F}) e^{i\frac{k}{2F}x_0^2} [2a\mathrm{sinc}(k_{x_0}a)], \tag{41}$$

which is also proportional to the sinc function. Since the square of a sinc function  $\operatorname{sinc}^2(x) = 0.5$  when x = 1.393, the FWHM of the focused plane wave in Eq. (41) is given by  $PR_{FWHM}^2 = 2x_0 \approx 0.8868\lambda F/D$ . Note that  $x = k_{x_0}a = kx_0a/F = 1.393$ , then  $x_0 = 1.393F/(ka) = 0.4434\lambda F/D$ , where D = 2a is the width of the 1D array transducer. Choosing F = 100 mm, D = 25 mm, f = 3.5 MHz, and c = 1500 m/s, then  $\lambda = c/f = 0.4286$  mm and  $PR_{FWHM}^2 = 1.5202$  mm (see Figs. 2(b) and 4(b)). Let  $\alpha = 2\pi/a = 0.5027$  mm<sup>-1</sup>, the center positions of the peaks of the radiation force will be  $k_{x_0} = kx_0/F = \pm \alpha$  or  $x_0 = \pm d = \pm F\alpha/k = \pm 2\pi F/(ka) = \pm 3.4286$  mm (see Figs. 2(b) and 4(b)). Thus, we have  $d_1 = d - (PR_{FWHM}^2/2) = 2.6685$  mm and  $d_2 = d + (PR_{FWHM}^2/2) = 4.1887$  mm (see Fig. 3(b)). With these parameters, line plots along  $x_0$  are give in Figs. 2(b) (pink dash-dotted line) and 4(b). As in the focused Bessel beam case in Subsection I.d above, a piecewise (binary) cosine aperture weighting can be used to increase transmit power to produce a stronger radiation force (see Ref. [19]), i.e., setting  $\cos(\alpha r_1) = 1$  if  $\cos(\alpha r_1) \ge 0$ , and  $\cos(\alpha r_1) = -1$  otherwise (see Figs 4(b), and Figs. 5(e) to 5(h)).

### 3. RESULTS

Fig. 1 illustrates how a focused shear wave can be produced with a focused Bessel beam (Fig. 1(a), with an annular or 2D array transducer) or a focused cosine beam (Fig. 1(b), with 1D array transducer) via a radiation force, and how it can be used to modulate imaging waves for low-sidelobe and high-contrast super-resolution imaging (Figs. 1(c) and 1(d)). Figs. 2(a) and 2(b) illustrate the super-resolution imaging process quantitatively with focused shear waves using typical parameters in medical ultrasound imaging, corresponding to Fig. 1(c) and 1(d) respectively. Figs. 3(a) and 3(b) show the resonance gains of focused shear waves produced with a focused Bessel beam and a focused cosine beam in Figs. 1(a) and 1(b) respectively. Figs. 4(a) and 4(b) are theoretical and simulation results of radiation forces produced with the focused Bessel beam and focused cosine beam in Figs. 1(a) and 1(b) respectively, using typical medical ultrasound imaging parameters. Figs. 5(a)-5(d) and 5(e)-5(h) are the simulation results of both transverse and axial profiles of radiation forces produced by the focused Bessel and cosine transducers in Figs. 1(a) and 1(b) respectively, using the parameters given in Figs. 4(a) and 4(b). Since there is a large depth of field in radiation forces (Figs. 5(b), 5(d), 5(f), and 5(h)), real-time 2D ( $x_0 - z$  plane) super-resolution imaging is possible. For detailed descriptions of the figures, the readers are referred to the legends of the figures.

# 4. CONCLUSION

Methods of producing modulators for low-sidelobe and high-contrast super-resolution imaging using focused shear waves generated remotely by a cylindrical ring or plates (or a focal spot of conventional focused beam) of radiation forces were studied in details both theoretically and with computer simulations. These shear waves may resonate to form large peaks under certain boundary conditions to increase signal-to-noise ratio (SNR), and can also be produced locally. If the modulated imaging waves can interfere coherently before being detected, the sensitivity and dynamic range, and thus the image resolution can be greatly increased (using small physical particles such as optically opaque ions as modulators, atomic imaging may be possible). The results show that it is feasible to produce focused shear waves as modulators for super-resolution imaging using typical parameters used in medical ultrasound. Because the cylindrical ring or plates of radiation forces have a large depth of field (Fig. 5), real-time 2D super-resolution imaging with focused shear waves is possible. The study in this paper opens up an opportunity for super-resolution imaging of mechanical properties (shear-wave amplitude, speed, spectrum, and nonlinearity) of biological soft tissues deep in the body, and may help to distinguish between benign and malignant tissues.

# **REFERENCES**

- [1] Ernst Abbe. "Beiträge zur Theorie des Mikroskops und der mikroskopischen Wahrnehmung." Archiv für mikroskopische Anatomie 9, no. 1 (1873): 413-468.
- [2] B. Xu, Z. Wang, and J. He. "Super-resolution imaging via aperture modulation and intensity extrapolation." *Scientific reports* 8, no. 1 (2018): 15216.
- [3] K. Gao, C. M. Donahue, B. G. Henderson, and R. T. Modrak. "SREMI: Super-resolution electromagnetic imaging with single-channel ground-penetrating radar." *Journal of Applied Geophysics* 205 (2022): 104777.
- [4] G. Lerosey, J. De Rosny, A. Tourin, and M. Fink. "Focusing beyond the diffraction limit with far-field time reversal." *Science* 315, no. 5815 (2007): 1120-1122.
- [5] R. Kumudham and V. Rajendran. "Super resolution enhancement of underwater sonar images." SN Applied Sciences 1, no. 8 (2019): 852.
- [6] W. Chen, H. Jiang, and X. Huang. "Super-resolution acoustic imaging." Applied Physics Letters 120, no. 11 (2022).
- [7] K. Prakash, B. Diederich, R. Heintzmann, and L. Schermelleh. "Super-resolution microscopy: a brief history and new avenues." Philosophical Transactions of the Royal Society A 380, no. 2220 (2022): 20210110.
- [8] P. Song, J. M. Rubin, and M. R. Lowerison. "Super-resolution ultrasound microvascular imaging: Is it ready for clinical use?." Zeitschrift für Medizinische Physik (2023).
- [9] K. Christensen-Jeffries, O. Couture, P. A. Dayton, Y. C. Eldar, K. Hynynen, F. Kiessling, M. O'Reilly, G. F. Pinton, G. Schmitz, M. Tang, M. Tanter, and R. J. G. van Sloun, "Super-resolution ultrasound imaging." *Ultrasound in medicine & biology* 46, no. 4 (2020): 865-891.
- [10] O. Couture, V. Hingot, B. Heiles, P. Muleki-Seya, and M. Tanter. "Ultrasound localization microscopy and super-resolution: A state of the art." *IEEE transactions on ultrasonics, ferroelectrics, and frequency control* 65, no. 8 (2018): 1304-1320.
- [11] M. Fink and M. Tanter. "Multiwave imaging and super resolution." Physics today 63, no. 2 (2010): 28-33.
- [12] H. W. Jones, "Superresolution in ultrasonic imaging." Acoustical Imaging (1993): 71-76.
- [13] S. W. Hell and J. Wichmann. "Breaking the diffraction resolution limit by stimulated emission: stimulated-emission-depletion fluorescence microscopy." Optics letters 19, no. 11 (1994): 780-782.
- [14] E. Betzig, G. H. Patterson, R. Sougrat, O. W. Lindwasser, S. Olenych, J. S. Bonifacino, M. W. Davidson, J. Lippincott-Schwartz, and H. F. Hess. "Imaging intracellular fluorescent proteins at nanometer resolution." science 313, no. 5793 (2006): 1642-1645.
- [15] Jian-yu Lu, "Modulation of point spread function for super-resolution imaging." IEEE Transactions on Ultrasonics, Ferroelectrics, and Frequency Control, vol. 71, no. 1, pp. 153-177, January 2024.
- [16] Jian-yu Lu, "A general method to obtain clearer images at a higher resolution than theoretical limit," 186th Meeting of Acoustical Society of America, Acoustical Lay Language Paper (ALLP), April 22, 2024 (https://acoustics.org/a-general-method-to-obtain-clearer-images-at-a-higher-resolution-than-theoretical-limit/).
- [17] Jian-yu Lu, "Remote Super-Resolution Mapping of Wave Fields," *IEEE Transactions on Ultrasonics, Ferroelectrics, and Frequency Control*, vol. 72, no. 3, pp. 370-379, March 2025.
- [18] Jian-yu Lu, "Generation of modulators for super-resolution imaging," *Journal of Acoustical Society of America*, vol. 157 no. 4, pt. 2, pp. A56, 2025 (abs) (https://doi.org/10.1121/10.0037370).
- [19] Jian-yu Lu, "Focused limited-diffraction beams for ultrasound therapy applications," in 2021 IEEE International Ultrasonics Symposium Proceedings, pp.1-4, 2021.
- [20] Jian-yu Lu, "Producing Bessel beams with an RF transformer," IEEE Transactions on Ultrasonics, Ferroelectrics, and Frequency Control (publication date: August 21, 2025) (DOI: <a href="https://doi.org/10.1109/TUFFC.2025.3601216">https://doi.org/10.1109/TUFFC.2025.3601216</a>)
- [21] Jian-yu Lu, "Focused beams for high-resolution imaging and other applications." In *Proceedings of Meetings on Acoustics* (POMA), vol. 45, no. 1. AIP Publishing, 2021.
- [22] Jian-yu Lu, "Limited diffraction array beams," *International Journal of Imaging System and Technology*, vol. 8, no. 1, pp. 126-136, January 1997 (ISSN: 0899-9457)
- [23] M. Xu and L. V. Wang. "Photoacoustic imaging in biomedicine." Review of scientific instruments 77, no. 4 (2006).
- [24] J. Jodhani, A. Handa, A. Gautam, and R. Rana. "Ultrasonic non-destructive evaluation of composites: A review." Materials Today: Proceedings 78 (2023): 627-632.
- [25] K. Nightingale. "Acoustic radiation force impulse (ARFI) imaging: a review." Current medical imaging reviews 7, no. 4 (2011): 328-339.
- [26] S. Peter and R. I. Leine. "Excitation power quantities in phase resonance testing of nonlinear systems with phase-locked-loop excitation." Mechanical Systems and Signal Processing 96 (2017): 139-158.
- [27] G. T. Mase, R. E. Smelser, and G. E. Mase. Continuum mechanics for engineers. CRC press, 2009.
- [28] J. Bercoff, M. Tanter, and M. Fink. "Supersonic shear imaging: a new technique for soft tissue elasticity mapping." *IEEE transactions on ultrasonics, ferroelectrics, and frequency control* 51, no. 4 (2004): 396-409.
- [29] J. M. Kweun, H. J. Lee, J. H. Oh, H. M. Seung, and Y. Y. Kim. "Transmodal Fabry-Pérot resonance: theory and realization with elastic metamaterials." *Physical review letters* 118, no. 20 (2017): 205901.
- [30] Jian-yu Lu, "An experimental study of focused Bessel beams," in 2025 IEEE International Ultrasonics Symposium Proceedings, pp. 1-4, 2025 (in press).
- [31] J. W. Goodman. Introduction to Fourier optics. Roberts and Company publishers, 2005.
- [32] S. C. Gupta, "Delta function." IEEE Transactions on Education 1 (1964): 16-22.
- [33] J. D. Achenbach. Wave propagation in elastic solids. Elsevier, North-Holland Publishing Company, 1973.
- [34] P. M. Morse and H. Feshbach, Methods of Theoretical Physics. Part I, McGraw-Hill, New York, 1953.
- [35] I. S. Gradshteyn and I. M. Ryzhik, Table of Integrals, Series, and Products, 7th Edition, Academic Press, U.K., 2007.